Mixed-Cation Vacancy-Ordered Perovskites ($Cs_2Ti_{1-x}Sn_xX_6$; X = I, Br); Low Temperature Miscibility, Additivity and Tunable Stability

Shanti M. Liga[a,‡], Seán R. Kavanagh[b,c,‡], Aron Walsh[c,d], David O. Scanlon[b] & Gerasimos Konstantatos[a,e,*]

[a]ICFO-Institut de Ciències Fotòniques, The Barcelona Institute of Science and Technology, 08860 Castelldefels (Barcelona), Spain

[b]Thomas Young Centre and Department of Chemistry, University College London, London, UK

[c]Thomas Young Centre and Department of Materials, Imperial College London, London, UK

[d]Department of Physics, Ewha Womans University, Seoul 03760, Korea

[e]ICREA-Institució Catalana de Recerca i Estudis Avancats, Passeig Lluís Companys 23, 08010 Barcelona, Spain

[‡]These authors contributed equally: Shanti M. Liga, Seán R. Kavanagh

* Corresponding author, e-mail: gerasimos.konstantatos@icfo.es

Abstract

Lead toxicity and poor stability under operating conditions are major drawbacks impeding the widespread commercialization of metal halide perovskite solar cells. Ti(IV) has been considered as an alternative species to replace Pb(II) because it is relatively non-toxic, abundant and its perovskite-like compounds have demonstrated promising performance when applied in solar cells (η > 3%), photocatalysts and non-linear optical applications. Yet, Ti(IV) perovskites show instability in air, hindering their use. On the other hand, Sn(IV) has a similar cationic radius to Ti(IV), adopting the same vacancy-ordered double perovskite (VODP) structure and showing good stability in ambient conditions. We report here a combined experimental and computational study on mixed titanium-tin bromide and iodide VODPs, motivated by the hypothesis that these mixtures may show a higher stability than the pure titanium compositions. Thermodynamic analysis shows that the cations are highly-miscible in these vacancy-ordered structures. Experimentally, we synthesized mixed titanium-tin VODPs as nanocrystals across the entire mixing range *x* ($Cs_2Ti_{1-x}Sn_xX_6$; X = I or Br), using a colloidal synthetic approach. Analysis of the experimental and computed absorption spectra reveals weak hybridization and interactions between Sn and Ti octahedra, with the alloy absorption being essentially a linear combination of the pure Sn and Ti compositions. These compounds are stabilized at high percentages of Sn ($x \sim 60\%$), as expected, with bromide compositions demonstrating greater stability compared to the iodides. Overall, we find that these materials behave akin to molecular aggregates, with the thermodynamic and optoelectronic properties governed by the intra-octahedral interactions.

Introduction

The development of solution-processed optoelectronic materials based on abundant and non-toxic elements is of great interest for sustainable technological progress. In particular, lead halide perovskites are at present the best performing solution-processed photovoltaic materials, with a power conversion efficiency record of 26% in 2023.[1] Nevertheless, both the regulatory concerns due the presence of lead and poor stability under ambient operating conditions pose major barriers to their commercialization. Lead is toxic and when released from the perovskite structure into the soil it is 10 times more bioavailable than other natural lead sources.[2–4]

The exceptional optoelectronic properties of lead halide perovskites, along with these stability and toxicity drawbacks, have spurred major research interest in 'perovskite-inspired materials'.[5,6] These are materials with similar structural and/or chemical properties to the prototypical halide perovskites, but avoiding the presence of lead. Within the perovskite-structured subclass of these materials, ionic substitution is employed as a design principle, replacing Pb with a combination of chemically-similar cations.[7] Among these novel lead-free perovskites developed over the last decade, titanium-based vacancy-ordered double perovskites (VODPs)(Cs_2TiX_6; X = I, Br, Cl) have attracted particular attention following the recent demonstration of high performance in solar cell devices, with 3.3%[8] power conversion efficiency – the current best performance for a Sn- and Pb-free perovskite structure. The elemental abundance of Ti[9] and its low toxicity[10] make it a viable replacement for Pb.

Beyond photovoltaic applications, the A_2BX_6 structural family exhibit features associated with both zero-dimensional and three-dimensional materials (such as low thermal conductivity,[11] high compressibility and

strong exciton binding despite relatively small electronic band gaps),[12–15] makes them potential candidates for a range of alternative applications, such as potential thermoelectric materials,[11] white-light emitters / phosphors,[16,17] photocatalysts,[18] high-entropy semiconductors[19] and more, as well as offering a highly-tunable playground to study physical phenomena associated with strong Frenkel excitons.[12–15] Moreover, these materials have been reported to show non-linear optical activity, being in fact the only known third harmonic generation (THG) active lead-free perovskite structures.[20]

The stability of titanium-based vacancy-ordered perovskites has attracted significant debate. While the chloride (Cs_2TiCl_6) has been reported to show slow decomposition in air, only detectable after a couple of weeks,[20,21] for the bromide (Cs_2TiBr_6) and the iodide (Cs_2TiI_6) compositions, there is less consensus. Chen et al.[8] reported Cs_2TiBr_6 thin films to show stability in air, while Mendes et al. detected amorphous titanium oxide and cesium bromide on the surface of nascent large-grain Cs_2TiBr_6 samples.[22] Kong et al.,[21] Euvrard et al.[23] and He et al.[24] found moderate to fast decomposition rates when synthesized in powder form, and more recently Grandhi et al.[20] and Liga et al.[17,25,26] reported Cs_2TiBr_6 nanocrystal (NC) films to decompose within hours to minutes. Regarding Cs_2TiI_6, while Ju et al.[27] found that it is stable in powder form, Kupfer et al.[28] found the powder to be unstable and Liga et al.[25] observed fast decomposition of the NC films in air. The high instability in air for Ti-based vacancy-ordered perovskites significantly hinders the characterization of their properties (particularly for techniques which require contact with air) as well as their application in devices.

On the other hand, the Cs_2SnX_6; X = I, Br, Cl family have been shown to be mostly stable in air and under thermal, water and photo-stresses.[29–31] In fact, these compounds are the decomposition products typically witnessed for the unstable tin(II)-based ABX_3 single perovskites ($CsSnX_3$; X = I, Br, Cl). Consequently, this subclass has received much more research attention over the past few years, particularly when it comes to device applications.[32–35] The iodide (Cs_2SnI_6) has been found to show some instability under air, though with relatively slow decomposition, as Saporov et al.[30] reported cesium iodide (CsI) peaks appearing in x-ray diffraction (XRD) measurements after 60 days in air.

Since Sn and Ti have comparable ionic radii,[36] we hypothesized that mixing tin with titanium in the same host perovskite-like structure could stabilize the final mixed composition. Thus, we prepared mixed compositions of tin-titanium bromide and iodide VODPs ($Cs_2Ti_{1-x}Sn_xX_6$; X = I, Br) across the entire mixing range *x*, and studied their properties. We synthesized all the mixed compositions as colloidal nanocrystals (NCs) using the hot-injection method. We employed a combined approach, characterizing the properties of these materials both computationally and experimentally to elucidate the behavior and impact of cation mixing on the stability and optoelectronic properties of this series of novel vacancy-ordered double perovskites. While not the focus of this study, we note that the pure Sn and Ti chloride VODPs were also synthesized and characterized in our previous work,[12] and so the same computational analysis was performed for $Cs_2Ti_{1-x}Sn_xCl_6$ – appended to the SI (Figures S14 & S15).

Materials and Methods

Chemicals

Cesium acetate (CsAc 99.9% trace metals basis), titanium(IV) isopropoxide ($Ti(O\text{-}i\text{-}Pr)_4$, 97.0%), oleic acid (OA, technical grade 90%), 3-(N,N-dimethyl octadecylammonio)propanesulfonate (DMOP, 99.0%), bromotrimethylsilane (TMSBr, 97%) and acetone (99.5%) were purchased from Sigma-Aldrich. Tin(IV) acetate ($SnAc_4$ 98%) and iodotrimethylsilane (TMSI, 97%) were purchased from Fischer Scientific. Toluene (anhydrous, 99.8%) was purchased from Scharlabs. 1-octadecene (ODE, 90%) was purchased from Alfa Aesar. All chemicals were used without any further purification.

Experimental Methods

Preparation of cesium oleate solution. Cesium oleate was prepared following a previously reported method.[37] 0.768 g (4 mmol) of cesium acetate were loaded in a 50 ml three-neck flask together with 7.56 ml of OA and 18.72 ml of ODE. The solution was degassed through 3 cycles under argon and vacuum and heated at 110 °C for 30 minutes under argon. Afterwards, the solution was left under vacuum for 3 hours at 110 °C. The as-prepared solution was stored under nitrogen.

Synthesis of $Cs_2Ti_{1-x}Sn_xX_6$ NCs (X = I, Br).

Synthesis of Cs_2SnX_6. Cs_2SnX_6 (X = I, Br) NCs were prepared following our previously published procedure.[12] For the synthesis of Cs_2SnI_6 NCs, 112.8 mg of Sn(IV) acetate (0.31 mmol) and 60 mg of DMOP were weighed in the glovebox and loaded in a 50 ml three-neck flask together with 4 ml of the cesium oleate solution (0.62 mmol), 2 ml of ODE and 2 ml of OA. The solution was degassed through 3 cycles of argon and vacuum and heated at 110 °C for 35 minutes under vacuum. At this point, 273µL of TMSI (1.86 mmol) was injected under argon at 140 °C and the reaction was carried out for 20 seconds and then quenched by diluting the solution in 10 ml of toluene. The synthesis of Cs_2SnBr_6 NCs was carried out following the above procedure, except that the Cs:Sn:X precursors ratio used was 2:2:9 instead

of 2:1:6, which means that 225.6 mg (0.62 mmol) of Sn acetate and 380 µL (2.8 mmol) of TMSBr were used in the synthesis.

Synthesis of Cs_2TiX_6. For the synthesis of Cs_2TiX_6 (X = I, Br), 4 ml of cesium oleate (0.62 mmol) and 60 mg of DMOP were weighted in the glovebox and loaded in a 50 ml three-neck flask together with 2 ml of ODE, 2 ml of OA and 238 µl of titanium(IV) isopropoxide (0.78 mmol). The solution was degassed through 3 cycles of argon and vacuum and heated at 110 °C for 35 minutes under vacuum. At this point, for the case of Cs_2TiI_6 synthesis, 1238 µL (8.436 mmol) of TMSI was injected and after 20 seconds the reaction was quenched by diluting the solution in 10 ml of toluene. For the synthesis of Cs_2TiBr_6, 574 µL (4.218 mmol) of TMSBr was injected and the reaction was quenched as for Cs_2TiI_6 synthesis.

Synthesis of $Cs_2Ti_{1-x}Sn_xI_6$. Mixed titanium-tin iodide VODPs were prepared using the same method used for the preparation of pure tin and pure titanium VODP NCs. 4 ml of cesium oleate and 60 mg of DMOP were loaded in a 50 ml three-neck flask together with Sn(IV) acetate and Ti(IV) isopropoxide in different ratio, 2 ml of ODE and 2 ml of OA. Since the difference in precursor ratios between pure Cs_2TiI_6 and pure Cs_2SnI_6 was quite large (Cs:Ti:I = 2:2.5:27 and Cs:Sn:I = 2:1:6 respectively), the percentage concentrations of tin and titanium precursors in the sample names refer to their pure synthesis ratios, such that the 50% sample was synthesized using a precursor ratio of Cs:Ti:Sn:I = 2:1.25:0.5:27. For all the mixed phases, an iodine ratio of 27 was used to avoid the formation of CsI. Table S1 lists the precursor ratios used for all iodide alloy syntheses. The solution was degassed through 3 cycles of argon and vacuum and heated at 110 °C for 35 minutes under vacuum. At this point 1238 µL (8.436 mmol) of TMSI were injected and after 20 seconds the reaction was quenched by diluting the solution in 10 ml of toluene.

Synthesis of $Cs_2Ti_{1-x}Sn_xBr_6$ NCs. For the synthesis of mixed titanium-tin bromide VODPs, 4 ml of cesium oleate and 60 mg of DMOP were loaded in a 50 ml three-neck flask together with Sn(IV) acetate and Ti(IV) isopropoxide in different ratio (while the total Cs:B ratio was kept 2:2.5), 2 ml of ODE and 2 ml of OA. The solution was degassed through 3 cycles of argon and vacuum and heated at 110 °C for 35 minutes under vacuum. At this point, 574 µL (4.218 mmol) of TMSBr was injected and after 20 seconds the reaction was quenched by diluting the solution in 10 ml of toluene.

Washing of the NCs. In the first step of the washing procedure, 5 ml of methylacetate was added as antisolvent to 5 ml of all the NC solutions except for the case of Cs_2TiI_6, which does not need the addition of an antisolvent to precipitate during centrifugation and that decomposes into a whitish product in case of addition of it. The solutions were centrifuged at 5800 rpm for 10 minutes. Afterwards, the supernatant was discarded and the precipitate was redispersed in 4 ml of toluene. The solution was centrifuged again at 5800 rpm for 10 minutes and the supernatant again discarded while the precipitate redispersed in 3 ml of toluene. Finally, the solution was centrifuged at 1400 rpm for 4 minutes to remove possible aggregates and the supernatant was filtered using a 0.22 µm PTFE filter. The solutions were stored under inert atmosphere.

Computational Methods

To study the mixed compositions ($Cs_2Ti_{1-x}Sn_xX_6$; X = I, Br, Cl), the special quasi-random structure (SQS)[38] approach was employed, whereby supercells are generated with the Sn/Ti cations arranged 'quasi-randomly', such that the atomic pair correlation functions give as close a match as possible to that of an ideal infinite random distribution.[39] The use of this approach and assumption of random cation mixing is validated by the near-negligible mixing enthalpies observed (Figure 2), demonstrating minimal inter-octahedral interactions and thus negligible short-range ordering effects. The *icet* package[40,41] was used to generate 72-atom SQS supercells via a Monte Carlo simulated annealing algorithm, which gave a best objective function score (closest match to random cation distribution) with a non-diagonal expansion matrix of the 9-atom $Fm\bar{3}m$ primitive cell:

$$T = \begin{bmatrix} -1 & 0 & 0 \\ 0 & -2 & 2 \\ -2 & 2 & 2 \end{bmatrix}$$

The associated total energy calculations were performed primarily using Density Functional Theory (DFT) within the Vienna Ab Initio Simulation Package (VASP).[42] Scalar-relativistic pseudopotentials were employed to describe the interaction between core and valence electrons, via the projector-augmented wave (PAW) method.[43] The Cs_sv ($5s^25p^66s^1$), Sn_d ($4d^{10}5s^25p^2$), Ti_pv ($3p^64s^23d^2$), I ($5s^25p^5$), Br ($4s^24p^5$), and Cl ($3s^23p^5$) PAW potentials were used, with the parentheses listing the valence electron configurations of each. These choices were tested and validated in our previous work on the endpoint compositions (Cs_2SnX_6 & Cs_2TiX_6).[12]

The structural properties of these materials are well described with the HSE06 range-separated hybrid DFT functional[44] including dispersion corrections (Grimme's D3 with the recommended PBE0+BJ parametrizations)[45,46] to account for van der Waal's interactions between the isolated octahedra.[12] As such, the same computational setup was used for

the DFT calculations in this study, with a plane-wave energy cutoff of 300 eV and Γ-centered *k*-point sampling density of 0.27 $Å^{-1}$ in reciprocal space (corresponding to a *k*-point mesh of 3 × 3 × 3 for the 9-atom primitive unit cell), previously obtained using vaspup2.0[47] to give energies converged to <0.1 meV/atom. A convergence criterion of 0.01 eV/Å was imposed on the forces on each atom during structural relaxation, with relaxations continually iterated until cell volumes were unchanged, to avoid Pulay stress effects.

In analyzing the thermodynamics of cation mixing, the enthalpy of mixing (ΔH_{mix}) is defined as:

$$\Delta H_{mix} = E_{Cs_2Sn_xTi_{1-x}X_6} - (x(E_{Cs_2SnX_6}) + (1-x)(E_{Cs_2TiX_6}))$$

where $E_{Cs_2Sn_xTi_{1-x}X_6}$ is the energy per atom of the mixed system, $E_{Cs_2SnX_6}$ and $E_{Cs_2TiX_6}$ are the energies per atom of the pure-phase Sn and Ti endpoint compositions, and *x* is the Sn mixing fraction in $Cs_2Ti_{1-x}Sn_xX_6$; X = I, Br, Cl. The entropy of mixing ΔS_{mix} was computed considering the configurational entropy contribution, given by the equation:

$$\Delta S_{mix} = -k_B(x ln(x) + (1-x)\ln(x))$$

where *x* is the cation mixing fraction as above and ΔS_{mix} is the configurational entropy *per mixed site.* Note that this equation assumes random cation mixing in the alloyed material, and this approximation is validated by the extremely low mixing enthalpies computed (see Results).

Electronic band structures and independent-particle optical absorption spectra were calculated with the HSE06 hybrid DFT functional, including spin–orbit coupling effects (HSE06+SOC) due to the presence of heavy-atom elements – see Kavanagh et al.[12] and Cucco et al.[48] for discussions on the impact of SOC on the electronic structure of these materials. For optical calculations, the number of empty virtual states was increased using vaspup2.0[47] until the high-frequency dielectric constant ε_∞ was converged to a precision of 0.01, and tetrahedron *k*-point smearing was used. Electronic densities of states (Figures S4 & S5) and unfolded band structures (Figures S6 & S7) were plotted using sumo[49] and easyunfold[50] respectively.

To analyze the intrinsic thermodynamic stability of these vacancy-ordered perovskites, the CompetingPhases module of the doped[51] defects analysis package was used to query the Materials Project and identify all compositions bordering the chemical stability region of the material within the given Cs – M – X (M = Sn, Ti; X = I, Br, Cl) chemical system. Within these bordering phases, all polymorphs with energies above hull less than 0.1 eV/atom according to the Materials Project[52] energies (doped default) were then re-relaxed using the HSE06 hybrid DFT functional including van der Waal's dispersion corrections (D3)[45,46] with the same plane-wave energy cutoff as before (300 eV), and converged kpoint sampling determined using vaspup2.0[47] in each case. Notably, the $Pm\bar{3}m$ polymorph was found to be the groundstate for all CsX (X = I, Br, Cl) with our HSE06+D3 model in agreement with experiment, despite this phase being 0.03 eV/atom above the convex hull according to the Materials Project database, demonstrating the importance of considering all phases within a reasonable error range of the convex hull when pulling initial structures from databases. For the extrinsic decomposition pathways, a similar workflow was followed where all bordering phases in the Cs – M – X – H – O (M = Sn, Ti; X = I, Br, Cl) chemical system, with energies above hull < 0.1 eV/atom, were pulled from the Materials Project using doped, and re-relaxed with HSE06+D3 with the same energy cutoff and converged kpoint sampling. Additionally, using the ComputedReaction class in pymatgen,[53] potential exothermic decomposition reactions of Cs_2MX_6 (M = Sn, Ti; X = I, Br, Cl) in the presence of $H_2O_{(g)}$, $O_{2(g)}$ and/or $H_{2(g)}$ were screened using the Materials Project energies. For gaseous species (O_2, Cl_2, H_2O, HBr, HCl, HI), energies were determined by computing the internal energy of an isolated molecule in a 30×30×30 $Å^3$ cell, and adding the thermal enthalpic and entropic contributions as computed using vaspkit.[54] All gases were calculated in their magnetic groundstate (i.e. singlet (S = 0) in each case except for O_2 which has triplet (S = 1) spin in the groundstate). Partial pressure contributions to the internal energies of gaseous phases were computed using the ideal gas law relation:

$$\Delta U = k_B T \log_e(P)$$

The analysis and plotting functionalities of doped, pymatgen and mctools[55] were then used to analyze the thermodynamic stability and extrinsic decomposition calculations.[29] The vasppy package[56] was used to calculate the radial distribution functions of the relaxed mixed-cation supercells (Figure S3).

All computational data and analysis from this study is openly-available at https://doi.org/10.5281/zenodo.8348189.

Results and discussion

Structural and chemical characterization

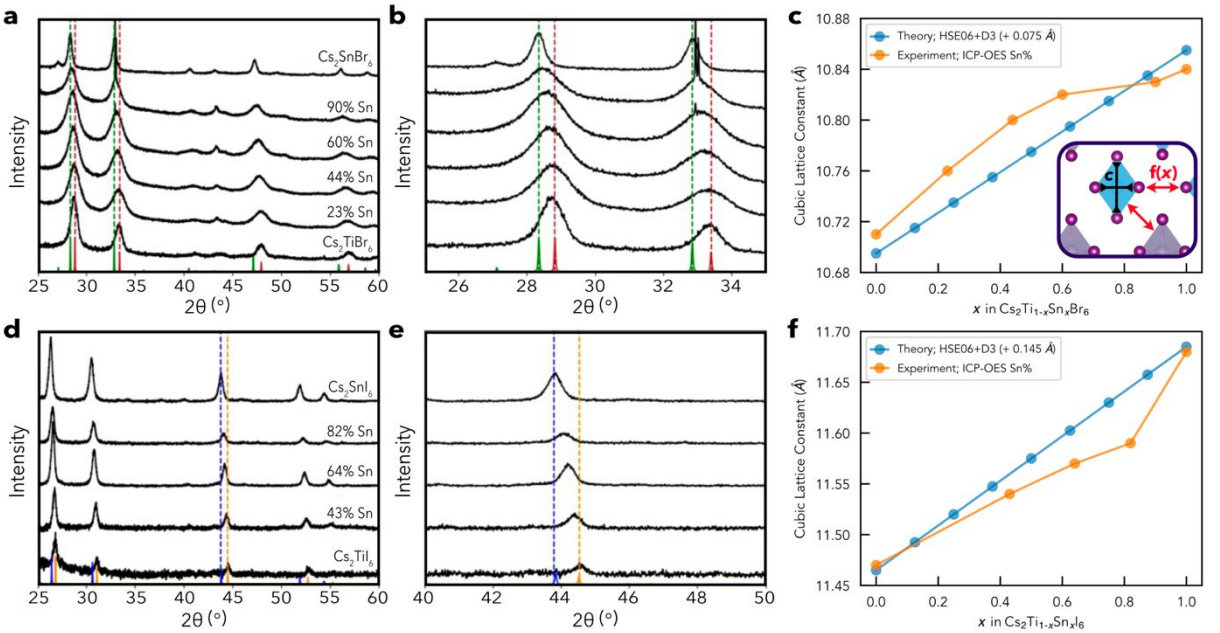

Figure 1. X-ray diffraction (XRD) patterns of (a) $Cs_2Ti_{1-x}Sn_xBr_6$ and (d) $Cs_2Ti_{1-x}Sn_xI_6$ nanocrystals (NCs). (b) and (e) are zoomed to the 25-35° and 40-50° ranges to observe the peak shifts with increasing tin fraction for (b) $Cs_2Ti_{1-x}Sn_xBr_6$ and (e) $Cs_2Ti_{1-x}Sn_xI_6$ NCs. In (a) and (b), the narrow peak at 32.97 degrees, which overlaps with the perovskite peak, originates from the silicon substrate. (c) and (f) show the trends in cubic lattice constant determined using Rietveld refinement of the XRD peaks, compared to that calculated using hybrid DFT for (c) $Cs_2Ti_{1-x}Sn_xBr_6$ and (f) $Cs_2Ti_{1-x}Sn_xI_6$, with rigid upshifts of +0.075 Å and +0.145 Å respectively to allow direct comparison of the trends. The crystal structure inset in (c) depicts the rigid intra-octahedral bond lengths and variable inter-octahedral atom distances.

Figure 1 (a) and (d) show the XRD patterns of the bromide alloys and iodide alloys respectively, measured in a nitrogen-filled sample holder. All the samples show $Fm\bar{3}m$ space group symmetry, as expected for vacancy-ordered double perovskites. Since Sn^{4+} (0.69 Å) is larger than that of Ti^{4+} (0.61 Å),[57] the lattice parameter increases by inserting more tin in the structure, so that all the diffraction peaks shift to lower angles as x in $Cs_2Ti_{1-x}Sn_xX_6$ increases. However, the difference in lattice parameters between pure titanium and pure tin compositions, both for the bromide (X = Br) and iodide (X = I), is quite small – around 0.2 Å for the iodide and 0.13 Å for the bromide, so this shift is visible only when zooming in to a narrower angular range (Figure 1 (b) and (e)).

Table 1. Lattice parameters and Sn % concentrations (x in $Cs_2Ti_{1-x}Sn_xX_6$) as measured by inductively-coupled plasma optical emission spectroscopy (ICP-OES) for each sample.

(a)

Sample name	Lattice par. (Å)	ICP-OES Sn%
Cs_2TiBr_6	10.706(3)	0
10%	10.761(5)	23
20%	10.800(2)	44
30%	10.819(6)	60
50%	10.831(4)	90
Cs_2SnBr_6	10.840(3)	100

(b)

Sample name	Lattice par. (Å)	ICP-OES Sn %
Cs_2TiI_6	11.468(5)	0
25% Sn	11.537(4)	43
50% Sn	11.5730(14)	64
75% Sn	11.594(5)	82
Cs_2SnI_6	11.6786(10)	100

The peaks of all the alloys are visibly broader than the pure Sn and Ti compositions, with Cs_2TiX_6 having larger full-width half-maximums (FWHMs) than Cs_2SnX_6. We believe that the different peak broadening in the diffraction pattern of the samples originate from the characteristic strain that the crystal lattice undergoes in NCs with different sizes and compositions. Indeed, the shape and size distribution of the NCs varied significantly with the composition, with, for instance, Cs_2SnI_6 showing a narrower size distribution and more symmetrical shapes than the mixed compositions and Cs_2TiI_6 (Figures S1 and S2), which would explain the narrower FWHM witnessed for Cs_2SnI_6. The strain has an effect not only on the width of the peaks but also on their position, which could therefore not be used to calculate the percentage of Sn using Vegard's law.

For this reason, the amount of Sn and Ti in the NC solutions were measured using inductively-coupled plasma optical emission spectroscopy (ICP-OES). Table 1 (a) and (b) lists the lattice parameters of each sample, extracted from Rietveld refinement (the refinement parameters are provided in Table S2) along with the percentage concentration of tin, where the Sn% corresponds to *x* in $Cs_2Ti_{1-x}Sn_xX_6$. For both halides (X = I, Br), the amount of tin that is incorporated to the NC (as measured by ICP-OES) is higher than the precursor ratio of tin loaded in the flask at the beginning of the synthesis (indicated under "Sample name" in the table), indicating that the formation of the Sn-based compound is more favorable than that of the Ti-based one.

Comparisons of the experimental and computed trends in the lattice parameters as a function of mixing ratio *x* are shown in Figure 1(c) and (f). In the idealized bulk computational model for these compounds, a perfectly-linear trend in the lattice parameters is predicted, in accordance with Vegard's law. We attribute the non-linearity in the experimental structure parameters to the nanocrystal strain effects described above. A small (~1%) systematic underestimation of the lattice parameter is witnessed with our static computational model, likely related to the neglect of thermal expansion in these calculations, and thus we apply rigid upshifts of +0.075 Å and +0.145 Å for the bromide and iodide respectively to allow direct comparison of the trends. A discussion on the performance of various DFT functionals in modelling the structural properties of $Cs_2(Sn/Ti)X_6$ is provided in Ref.12. As shown in Figure S3, analysis of the optimized crystal structures for the mixed compositions reveals that while the volume increases linearly and monotonically with increased Sn content, the *intra*-octahedral M-X bond lengths remain essentially fixed, with *d(Sn-X) & d(Ti-X)* in $Cs_2Ti_{1-x}Sn_xX_6$ retaining the same values as in Cs_2SnX_6 and Cs_2TiX_6. While *d(Sn-X) is* ~5% larger than *d(Ti-X)* for all X = I, Br, Cl, due to the larger ionic radius of Sn^{4+} compared to Ti^{4+},[12,57] the metal-halide bond lengths individually vary by less than 0.005 Å (~0.2%) within each $(Sn/Ti)X_6$ octahedron across the mixing range *x*. Instead, as depicted in the inset of Figure 1 I and shown in Figure S3, it is the vacant inter-octahedral space which is found to vary as the Sn/Ti ratio changes, while the differently-sized MX_6 octahedra behave as rigid building blocks with minimal disruption of local bonding environments upon mixing.

Computational analysis of the cation mixing thermodynamics confirmed that Sn- and Ti- vacancy-ordered perovskites are highly miscible. From hybrid Density Functional Theory (DFT) calculations of the mixed compositions, it was observed that the mixing enthalpies ΔH_{mix} for the Sn/Ti alloys are extremely low (Figure 2); <1 meV/mixed-site. A low energetic cost to cation mixing is to be expected in these vacancy-ordered structures consisting of isolated rigid octahedra, due to the extremely weak interactions between B-site cations (with metal-metal distances on the order of 8 Å) and negligible disruption of M-X bonding mentioned above. As discussed in Ref [12], the fully-oxidized cations (B^{+4} compared to B^{+2} in prototypical ABX_3 perovskites) here have essentially no *bonding* covalent interactions between B-site cations – aiding for instance, the emergence of ultra-strong excitons – and thus the mixing of *isovalent* species results in minimal disruption to both ionic and covalent bonding interactions, yielding almost "ideal mixture" behavior for the alloys. Consequently, the configurational entropy contribution ΔS_{mix} dominates the free energy of mixing ΔG_{mix} for these alloyed vacancy-ordered perovskites as shown in Figure 2, with cation mixing predicted to be thermodynamically favorable ($\Delta G_{mix} < 0$) at essentially all finite temperatures. Notably, this ideal mixing behavior explains and facilitates the recent low-temperature synthesis of high-entropy semiconductors from these vacancy-ordered perovskite compounds.[19]

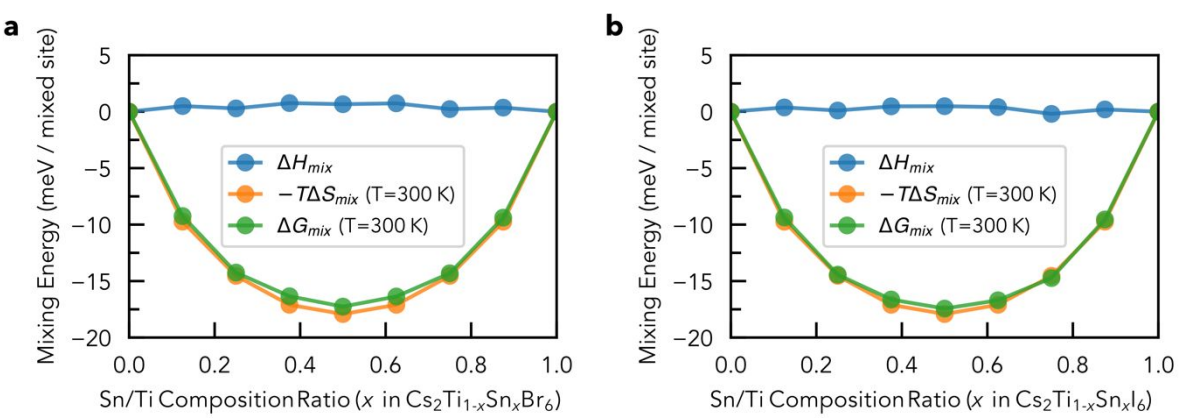

Figure 2. Calculated mixing enthalpies ΔH_{mix}, entropies ΔS_{mix} and free energies ΔG_{mix} as a function of the Sn/Ti composition ratio x in (a) $Cs_2Ti_{1-x}Sn_xBr_6$ and (b) $Cs_2Ti_{1-x}Sn_xI_6$ perovskites, at T = 300K.

Electronic and optical characterization

The measured absorption spectra of the bromide and iodide alloys, together with the pure titanium and tin spectra, are shown in Figure 3 (a) and (d), respectively. A key difference between the bromide and the iodide compounds is that, while the difference in bandgap between Cs_2TiBr_6 and Cs_2SnBr_6 is ~1.1 eV, the bandgap difference between Cs_2TiI_6 and Cs_2SnI_6 is only ~0.3 eV, and thus shows a smaller variation in the absorption onset wavelength. From the bromide absorption spectra, the samples containing up to 60% of tin still show the characteristic excitonic peaks of the $TiBr_6^{-2}$ octahedra in Cs_2TiBr_6,[12] and only when 90% of titanium is replaced by tin these peaks are not visible anymore. The same behavior is witnessed for the iodide alloys, where the excitonic peaks of the TiI_6^{-2} octahedra in Cs_2TiI_6 remain visible at the highest mixed Sn fraction of 82%. Consequently, the absorption onset energy remains effectively constant as Sn^{4+} is mixed into the Ti-based compounds, all the way up to alloys with a high Sn^{+4} mixing percentage (>80%), until the low energy Ti excitonic peaks disappear.

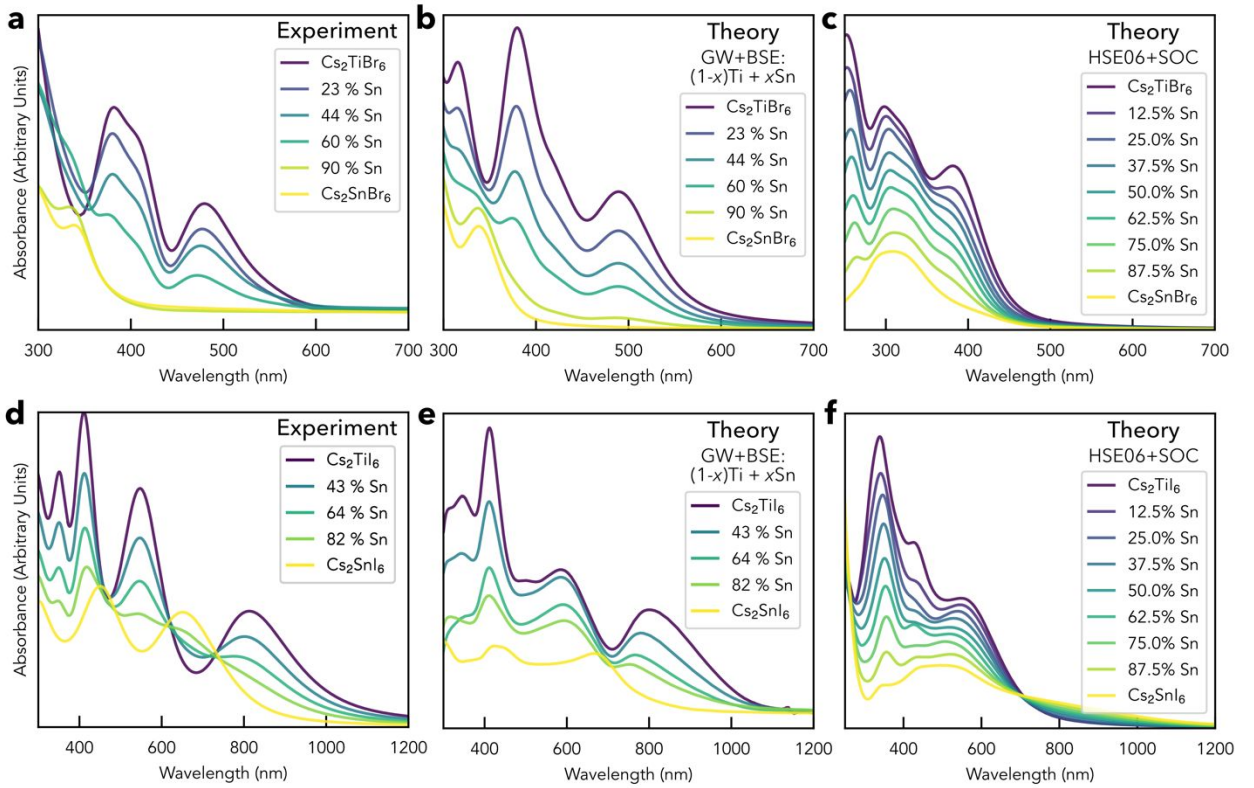

Figure 3. Measured and computed absorption spectra of (a-c) $Cs_2Ti_{1-x}Sn_xBr_6$ NC solutions and (d-f) $Cs_2Ti_{1-x}Sn_xI_6$ NC solutions. (b) and (e) show the expected absorption spectra from taking a linear combination of the pure phase spectra computed using GW+BSE (including excitonic effects) reported in Kavanagh et al., [12] while (c) and (f) show the explicitly-calculated independent-particle (excluding excitonic effects) absorption spectra of the mixed-cation supercells with hybrid DFT (HSE06) including spin-orbit coupling. Absorption spectra in (a,b,d,e) have been individually renormalised, while those in (c,f) have not, and so the relative spectral intensities for different mixed compositions in (c,f) are physically meaningful.

Likewise, in the independent-particle absorption spectra of the mixed compounds calculated using hybrid DFT with spin-orbit coupling (HSE06+SOC)(Figure 3c,f**Error! Reference source not found.**), we find minimal peak shifting or mixing, with the total absorption essentially being a linear combination of the tin and titanium related absorption features, weighted by the mixing fraction *x*. These calculations reveal that Ti-rich compounds have much stronger absorption intensity than the Sn-rich vacancy-ordered perovskites – due to reduced band dispersion and increased number of electronic states for Ti *d* vs Sn *s* (i.e. 10 vs 2)[12] which contributes to the dominance of the TiX_6 excitonic peaks in the absorption spectra of the mixed compounds even at very low percentage concentrations of Ti. While these single-particle spectra individually are not quantitatively reliable due to the presence of strong excitonic effects as shown in our previous work,[12] they allow us to qualitatively assess the impact of cation mixing on the quasi-particle electronic structure – here demonstrating additive behavior and minimal hybridization. The lack of cation orbital mixing or hybridization is further exemplified by the electronic densities of states (DOS) and band structure plots in Figures S4-7, which show negligible hybridization of the Ti *d* and Sn *s* states, with only their relative intensity varying as a function of the Sn fraction *x*. If we take these insights and plot the linear sum of the pure-phase excitonic absorption spectra, previously calculated using GW+BSE@HSE06+SOC,[12] we in fact find a good match with the experimentally-measured

spectra of the alloyed materials (Figure 3b,e**Error! Reference source not found.**) despite the naivety of this approach, further demonstrating the molecular aggregate type nature of this family. The validity of this approach here is further demonstrated by comparing the explicitly-computed independent-particle (HSE06+SOC) absorption spectra of the mixed-cation supercells with the linear sum of the pure Sn/Ti absorption spectra, shown in Figure S8, where almost identical spectra are obtained apart from some small differences due to weak halide band broadening in the mixed-cation supercells. We note here that explicit GW+BSE calculations for the 72-atom mixed-cation supercells used in this work are far from computationally tractable, with such calculations already at the limit of current computational capacity with the 9-atom unit cells of the pure-phase materials.

Overall, we see that the absorption features of the pure Sn and Ti-based phases are maintained in the spectra of the mixed compositions, both experimentally and computationally, where the strong titanium peaks dominate until the Ti fraction drops below a certain concentration threshold at which the tin-based features emerge. This somewhat-uncommon behavior can again be ascribed to the weak and non-covalent metal-metal interactions in these systems, arising from the effectively zero-dimensional crystal structure with isolated BX_6^{-2} octahedra. The lack of covalent metal-metal interactions in these vacancy-ordered perovskites results in minimal orbital hybridization or tuning of the electronic structure upon cation mixing, yielding this additive behavior for the properties of the mixed compositions – as also witnessed in Ref.19.

Stability

To study the ambient stability of the synthesized alloys, they were exposed to air and their XRD patterns were measured after several time intervals. Pure titanium VODPs were found to decompose within the time of the XRD measurement (around 10 minutes), so that only CsBr and CsI (for the bromide and iodide respectively) are visible when measuring their XRD in air (Figure S9). Focusing on the bromide alloys, with the 23% and 44% tin compositions, CsBr diffraction peaks appeared from the first minutes of air exposure. At this point the VODP peaks are still visible, though slightly shifted to lower angles suggesting a preferential loss of Ti over Sn from the mixed structure (Figure S10). As expected, when the tin content is increased to 60%, the stability increases significantly to 5-8 hours in air (Figure S11a).

Table 2 Calculated decomposition reactions and free energies for (a) Cs_2SnX_6 (X = I, Br) and (b) Cs_2TiX_6 in vacuum, and in the presence of oxygen and water, at T=300K. For oxidation reactions, the partial pressure of O_2 has been taken as that in air (0.2095 atm).

(a)

Reactants	Products	ΔG (eV)
Intrinsic Decomposition		
Cs_2SnI_6	$SnI_4 + CsI$	+0.477
Cs_2SnBr_6	$SnBr_4 + CsBr$	+1.107
Oxidation		
$Cs_2SnI_6 + O_{2(g)}$	$SnO_2 + 2CsI + 4I_{(s)}$	-2.43
$Cs_2SnBr_6 + O_{2(g)}$	$SnO_2 + 2CsBr + 2Br_{2(l)}$	-0.10
Hydration		
$Cs_2SnI_6 + 2H_2O$	$SnO_2 + 2CsI + 4HI_{(g)}$	+2.56 ($p_{(HI)} = 1$ atm) -0.99 ($p_{(HI)} = 10^{-15}$ atm)
$Cs_2SnBr_6 + 2H_2O$	$SnO_2 + 2CsBr + 4HBr_{(g)}$	+2.49 ($p_{(HBr)} = 1$ atm) -1.06 ($p_{(HBr)} = 10^{-15}$ atm)

(b)

Reactants	Products	ΔG (eV)
Intrinsic Decomposition		
Cs_2TiI_6	$TiI_4 + CsI$	+0.567
Cs_2TiBr_6	$TiBr_4 + CsBr$	+1.017
Oxidation		
$Cs_2TiI_6 + O_{2(g)}$	$TiO_2 + 2CsI + 4I_{(s)}$	-4.49
$Cs_2TiBr_6 + O_{2(g)}$	$TiO_2 + 2CsBr + 2Br_{2(l)}$	-1.70
Hydration		
$Cs_2TiI_6 + 2H_2O$	$TiO_2 + 2CsI + 4HI_{(g)}$	+0.49 ($p_{(HI)} = 1$ atm) -3.05 ($p_{(HI)} = 10^{-15}$ atm)
$Cs_2TiBr_6 + 2H_2O$	$TiO_2 + 2CsBr + 4HBr_{(g)}$	+0.88 ($p_{(HBr)} = 1$ atm) -2.67 ($p_{(HBr)} = 10^{-15}$ atm)

Since it has been reported that the instability of these vacancy-ordered perovskites in air is higher in humid atmosphere due to their hygroscopic nature,[24,26] we also tested storing this 60%-Sn bromide sample in a desiccator with 5% humidity. Under these conditions, the same sample was stable for over a week, while a CsBr diffraction peak became visible after 2 weeks (Figure S11b). The same experiments were carried out for the iodide alloys with similar trends observed, though the iodides are in general less stable than the bromides. Indeed, only the alloy containing 82% Sn was found to be stable for longer than a few minutes, though after 1 hour a CsI peak was clearly visible in the XRD pattern, even when storing the sample in a desiccator with 5% humidity (Figure S9).

The thermodynamic stability of these compounds was also computed using hybrid DFT, with the results tabulated in Table 2. Firstly, we find that all $Cs_2(Sn/Ti)X_6$ (X = I, Br) are thermodynamically stable with respect to decomposition into their competing phases within the Cs-Sn/Ti-X chemical space (i.e. stable in vacuum), as indicated by the positive (endothermic) decomposition energies for the intrinsic decomposition reactions, matching experimental observations of stability under inert atmospheres (Figure 1 (a) and (d) and Figures S9, S12). In agreement with thermogravimetric analysis (TGA) experiments[8,21,23,24,30] and semi-local DFT calculations from Ju et al.[27] and Liu et al.[58] for Cs_2TiI_6 and $Cs_2TiI_{6-x}Br_x$ respectively, we find that MX_4 and CsX (M = Sn, Ti; X = I, Br) are the lowest energy intrinsic decomposition products. The chemical stability regions showing the competing phases and chemical potentials within the Cs-Sn/Ti-X phase space are plotted in Figure S13, with much narrower stability regions for the iodides as expected. We note here that van der Waals dispersion interactions between the isolated octahedra are found to contribute significantly to the stability of these compounds.[12] Using hybrid DFT (HSE06) *without* the D3 vdW dispersion correction to perform geometry relaxations and total energy calculations, we find decomposition energies 378 and 216 meV *lower* for Cs_2SnI_6 and Cs_2TiI_6 respectively.

In the presence of oxygen however, we find that oxidation to SnO_2/TiO_2 is highly thermodynamically-favorable, with negative (exothermic) decomposition energies. In the presence of water, we find that the most favorable aqueous decomposition reaction is $Cs_2MX_6 + 2H_2O \rightarrow MO_2 + CsX + 4HX_{(g)}$; M = Sn, Ti; X = I, Br; in agreement with the conclusions of He et al.[24] Due to the formation of gaseous $HX_{(g)}$ (X = I, Br) as a reaction product in this case, the free energy of this decomposition is dependent on the partial pressure of $HX_{(g)}$ in the reaction environment, as shown in Table 2 and plotted in Figure 4. The effect of the gaseous product partial pressure on the reaction equilibrium indicates that aqueous decomposition will be inhibited in closed containers. Our decomposition energies qualitatively match those calculated by Kaewmeechai et al.[59] for Cs_2TiX_6, however their calculations did

not include gas partial pressure contributions (thus corresponding to p_{HX} = 1 atm for H_2O decomposition) which dictate the aqueous decomposition energies.

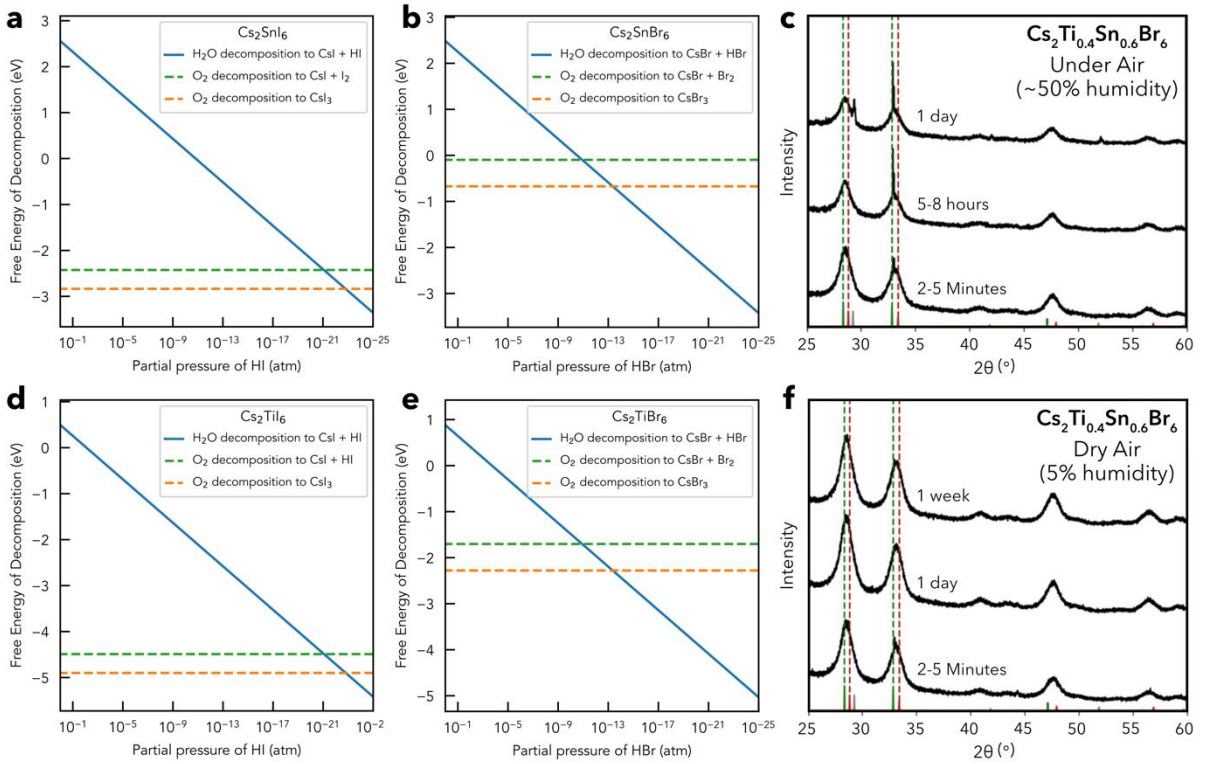

Figure 4. Calculated free energy of decomposition as a function of partial pressure of $HX_{(g)}$ for (a) Cs_2SnI_6, (b) Cs_2SnBr_6, (d) Cs_2TiI_6 and (e) Cs_2TiBr_6 at T=300K. For oxidation reactions, the partial pressure of O_2 has been taken as that in air (0.2095 atm). (c,f) Evolution of measured XRD patterns for the 60% Sn alloy of $Cs_2Ti_{1-x}Sn_xBr_6$ after (a) exposure to air (~50% humidity) and (b) when stored in a desiccator with 5% humidity. The narrow peak at 32.97° originates from the silicon substrate.

In agreement with the experimental observations, we find that stability increases as we move up the halogen periodic group from iodine to bromine, and the Sn VODPs are more stable than the Ti-based compounds, for both oxygen and aqueous decomposition. The greater instability of Cs_2TiX_6 compared to Cs_2SnX_6 is attributed to the stronger thermodynamic driving force (more exothermic formation energy) for TiO_2 compared to SnO_2. Given the large (~1.5 eV) difference in free energies of decomposition for Sn and Ti vacancy-ordered perovskites compared to the configurational entropy contribution for cation mixing (~20 meV), the thermodynamic stabilities of the alloys are predicted to follow the linear combination of the pure tin and titanium phases, weighted by the mixing fraction *x*, such that:

$$\Delta G_{Cs_2Sn_xTi_{1-x}X_6} = x(\Delta G_{Cs_2SnX_6}) + (1-x)(\Delta G_{Cs_2TiX_6}) + \Delta G_{mix} \approx x(\Delta G_{Cs_2SnX_6}) + (1-x)(\Delta G_{Cs_2TiX_6})$$

Thus a greater Sn fraction in the alloyed composition is predicted to yield increased stability with respect to decomposition in air and water, as witnessed experimentally. While empirically we expect more rapid decomposition with more exothermic (negative) reaction energies, we note that these calculations do not account for reaction *kinetics*. The hygroscopic nature of these compounds suggests that surface hydration could have a catalytic effect on decomposition rates, contributing to the accelerated decomposition in humid environments.

Conclusions

In summary, we have studied a series of novel lead-free vacancy-ordered double perovskites (VODPs) based on titanium and tin, with chemical formula $Cs_2Ti_{1-x}Sn_xX_6$ (X = I, Br). We have synthesized these alloys as nanocrystals (NCs) following a colloidal route, and characterized their structural, electronic, optical and thermodynamic properties using a combined experimental and computational approach. We have also computationally characterized the mixed-cation chloride VODPs (x = Cl; Figures S14 & S15) finding consistent trends in behavior. We find all phases to retain $Fm\bar{3}m$ symmetry, with lattice parameters slightly increasing in going from pure

titanium to pure tin compositions. In agreement with our experimental observations, calculations reveal the B-site cations to be highly-miscible in this structure, with BX_6^{-2} octahedra behaving as rigid blocks and the vacant inter-octahedral space varying to accommodate the changes in cation (octahedron) sizes.

We show that the mixed compositions have absorption features essentially equal to the linear combination of the pure Sn and Ti VODP phases, with this behavior ascribed to the lack of orbital mixing and weak interactions between the isolated BX_6^{-2} octahedra in the effectively zero-dimensional crystal structure. From XRD measurements over time in air, we observe that Cs_2SnX_6 NCs are stable in air while Cs_2TiX_6 NCs show decomposition after a few minutes of air exposure. Moreover, we observed that stability increases with higher values of x in $Cs_2Ti_{1-x}Sn_xX_6$ as expected and predicted computationally, with the bromide mixtures showing higher stability compared to the iodide ones.

Overall, our results further elucidate the unique properties of these compounds, where much of their behavior is reminiscent of molecular aggregates,[60] despite a three-dimensional structural connectivity in the solid. The combination of facile cation mixing and weak octahedral interactions / orbital hybridization demonstrated in this work, with resultant intriguing optoelectronic properties such as strong excitonic binding, could lend itself to several alternative applications beyond those mentioned in the introduction. One example is potential hosts for photoluminescent defects with quantum computing applications, for which minimal interaction with the host environment is desired for long coherence times.[61] Another is high-entropy semiconductors with low-temperature synthesis routes, aided by the ready miscibility of the cation site – as recently demonstrated in Ref.19.

Supporting Information

Experimental characterization methods and Rietveld refinement parameters; TEM analysis; computational structural (RDFs), electronic (densities of states and unfolded band structures) and optical (hybrid DFT absorption spectra) analysis; XRD patterns after exposure to various environments; calculated chemical stability regions (chemical potentials); computational analysis of $Cs_2Ti_{1-x}Sn_xCl_6$ vacancy-ordered perovskites.

Acknowledgements

S.R.K. acknowledges the EPSRC Centre for Doctoral Training in the Advanced Characterisation of Materials (CDT-ACM) (EP/S023259/1) for funding a Ph.D. studentship. D.O.S. acknowledges support from the EPSRC (EP/N01572X/1) and from the European Research Council, ERC (Grant 758345). The authors acknowledge the use of the UCL Kathleen High Performance Computing Facility (Kathleen@UCL), the Imperial College Research Computing Service, and associated support services in the completion of this work. Via membership of the UK's HEC Materials Chemistry Consortium, which is funded by the EPSRC (EP/L000202, EP/R029431, and EP/T022213), this work used the ARCHER2 UK National Supercomputing Service (www.archer2.ac.uk) and the UK Materials and Molecular Modelling (MMM) Hub (Thomas EP/P020194 and Young EP/T022213). The authors acknowledge financial support from the European Research Council (ERC) under the European Unions Horizon 2020 research and innovation program (Grant Agreement 725165) as well as from the European Unions Horizon 2020 research and innovation program under Marie Skodowska-Curie Grant Agreement 713729. This project has received funding also from the Spanish State Research Agency, through the Severo Ochoa Center of Excellence (CEX2019-000910-S), the CERCA Programme/Generalitat de Catalunya and Fundacio Mir-Puig. The authors also acknowledge funding by the Fundacio Joan Ribas Araquistain (FJRA). This project was funded also by EQC2019-005797-P (AEI/FEDER UE).

References

(1) *Best Research-Cell Efficiency Chart | Photovoltaic Research | NREL*. https://www.nrel.gov/pv/cell-efficiency.html (accessed 2023-07-16).

(2) Flora, G.; Gupta, D.; Tiwari, A. Toxicity of Lead: A Review with Recent Updates. *Interdisciplinary Toxicology* **2012**, *5* (2), 47–58. https://doi.org/10.2478/v10102-012-0009-2.

(3) Babayigit, A.; Duy Thanh, D.; Ethirajan, A.; Manca, J.; Muller, M.; Boyen, H. G.; Conings, B. Assessing the Toxicity of Pb-and Sn-Based Perovskite Solar Cells in Model Organism Danio Rerio. *Scientific Reports* **2016**, *6*, 1–11. https://doi.org/10.1038/srep18721.

(4) Li, J.; Cao, H.-L.; Jiao, W.-B.; Wang, Q.; Wei, M.; Cantone, I.; Lü, J.; Abate, A. Biological Impact of Lead from Halide Perovskites Reveals the Risk of Introducing a Safe Threshold. *Nat. Commun.* **2020**, *11* (1), 310. https://doi.org/10.1038/s41467-019-13910-y.

(5) Huang, Y. T.; Kavanagh, S. R.; Scanlon, D. O.; Walsh, A.; Hoye, R. L. Z. Perovskite-Inspired Materials for Photovoltaics and beyond-from Design to Devices. *Nanotechnology* **2021**, *32*(13), 132004. https://doi.org/10.1088/1361-6528/abcf6d.

(6) Savory, C. N.; Walsh, A.; Scanlon, D. O. Can Pb-Free Halide Double Perovskites Support High-Efficiency Solar Cells? *ACS Energy Lett* **2016**, *1* (5), 949–955. https://doi.org/10.1021/acsenergylett.6b00471.

(7) Akkerman, Q. A.; Manna, L. What Defines a Halide Perovskite? *ACS Energy Lett.* **2020**, *5*(2) 604–610. https://doi.org/10.1021/acsenergylett.0c00039.

(8) Chen, M.; Ju, M. G.; Carl, A. D.; Zong, Y.; Grimm, R. L.; Gu, J.; Zeng, X. C.; Zhou, Y.; Padture, N. P. Cesium Titanium(IV) Bromide Thin Films Based Stable Lead-Free Perovskite Solar Cells. *Joule* **2018**, *2* (3), 558–570. https://doi.org/10.1016/j.joule.2018.01.009.

(9) Morgan, J. W.; Anders, E. Chemical Composition of Earth, Venus, and Mercury. *Proceedings of the National Academy of Sciences* **1980**, *77* (12), 6973–6977. https://doi.org/10.1073/pnas.77.12.6973.

(10) Nuss, P.; Eckelman, M. J. Life Cycle Assessment of Metals: A Scientific Synthesis. *PLoS One* **2014**, *9* (7), 1–12. https://doi.org/10.1371/journal.pone.0101298.

(11) Bhumla, P.; Jain, M.; Sheoran, S.; Bhattacharya, S. Vacancy-Ordered Double Perovskites Cs2BI6(B = Pt, Pd, Te, Sn): An Emerging Class of Thermoelectric Materials. *Journal of Physical Chemistry Letters* **2022**, *13* (50), 11655–11662. https://doi.org/10.1021/acs.jpclett.2c02852.

(12) Kavanagh, S. R.; Savory, C. N.; Liga, S. M.; Konstantatos, G.; Walsh, A.; Scanlon, D. O. Frenkel Excitons in Vacancy-Ordered Titanium Halide Perovskites (Cs2TiX6). *Journal of Physical Chemistry Letters* **2022**, *13* (47), 10965–10975. https://doi.org/10.1021/acs.jpclett.2c02436.

(13) Cucco, B.; Katan, C.; Even, J.; Kepenekian, M.; Volonakis, G. Fine Structure of Excitons in Vacancy-Ordered Halide Double Perovskites. *ACS Mater. Lett.* **2023**, *5* (1), 52–59. https://doi.org/10.1021/acsmaterialslett.2c01010.

(14) Zhang, F.; Gao, W.; Cruz, G. J.; Sun, Y.; Zhang, P.; Zhao, J. Giant Excitonic Effects in Vacancy-Ordered Double Perovskites. *Physical Review B* **2023**, *107* (23), 235119. https://doi.org/10.1103/PhysRevB.107.235119.

(15) Biega, R.I.; Chen, Y.; Filip, M. R.; Leppert, L. Chemical Mapping of Excitons in Halide Double Perovskites. *arXiv preprint* **2023**, *2306* (11352). https://doi.org/10.48550/arXiv.2306.11352.

(16) Bhat, A. A.; Khandy, S. A.; Ali, A. M.; Tomar, R. Photoluminescence Emission Studies on a Lanthanum-Doped Lead Free Double Halide Perovskite, La:Cs_2SnCl_6. *J. Phys. Chem. Lett.* **2023**, *14*, 5004–5012. https://doi.org/10.1021/acs.jpclett.3c00522.

(17) Abfalterer, A.; Shamsi, J.; Kubicki, D. J.; Savory, C. N.; Xiao, J.; Divitini, G.; Li, W.; Macpherson, S.; Gałkowski, K.; Macmanus-Driscoll, et al. Colloidal Synthesis and Optical Properties of Perovskite-Inspired Cesium Zirconium Halide Nanocrystals. *ACS Mater. Lett.* **2020**, *2* (12), 1644–1652. https://doi.org/10.1021/acsmaterialslett.0c00393.

(18) Zhou, J.; Wu, D.; Tian, C.; Liang, Z.; Ran, H.; Gao, B.; Luo, Z.; Huang, Q.; Tang, X. Novelty All-Inorganic Titanium-Based Halide Perovskite for Highly Efficient Photocatalytic CO_2 Conversion. *Small* **2023**, *2207915*. https://doi.org/10.1002/smll.202207915.

(19) Folgueras, M. C.; Jiang, Y.; Jin, J.; Yang, P. High-Entropy Halide Perovskite Single Crystals Stabilized by Mild Chemistry. *Nature* **2023**, *621*, 282–288. https://doi.org/10.1038/s41586-023-06396-8.

(20) Grandhi, G. K.; Matuhina, A.; Liu, M.; Annurakshita, S.; Ali-Löytty, H.; Bautista, G.; Vivo, P. Lead-Free Cesium Titanium Bromide Double Perovskite Nanocrystals. *Nanomaterials* **2021**, *11* (6). https://doi.org/10.3390/nano11061458.

(21) Kong, D.; Cheng, D.; Wang, X.; Zhang, K.; Wang, H.; Liu, K.; Li, H.; Sheng, X.; Yin, L. Solution Processed Lead-Free Cesium Titanium Halide Perovskites and Their Structural, Thermal and Optical Characteristics. *J. Mater. Chem. C* **2020**, *8* (5), 1591–1597. https://doi.org/10.1039/c9tc05711k.

(22) Mendes, J. L.; Gao, W.; Martin, J. L.; Carl, A. D.; Deskins, N. A.; Granados-Focil, S.; Grimm, R. L. Interfacial States, Energetics, and Atmospheric Stability of Large-Grain Antifluorite Cs_2TiBr_6. *J. Phys. Chem. C* **2020**, *124* (44), 24289–24297. https://doi.org/10.1021/acs.jpcc.0c08719.

(23) Euvrard, J.; Wang, X.; Li, T.; Yan, Y.; Mitzi, D. B. Is Cs_2TiBr_6 a Promising Pb-Free Perovskite for Solar Energy Applications? *J. Mater. Chem. A* **2020**. https://doi.org/10.1039/c9ta13870f .

(24) He, Y.; Guo, X.; Zheng, H.; Xv, L.; Li, S. Stability Investigation of the Titanium-Based Eco-Friendly Perovskite-like Antifluorite Cs_2TiBr_6. *J. Mater. Chem. C* **2022**, *10* (24), 9301–9309. https://doi.org/10.1039/d2tc00729k.

(25) Liga, S. M.; Konstantatos, G. Colloidal Synthesis of Lead-Free $Cs_2TiBr_{6-x}I_x$ Perovskite Nanocrystals. *J. Mater. Chem. C* **2021**, *9* (34), 11098–11103. https://doi.org/10.1039/D1TC01732B .

(26) Liga, S. M.; Wang, Y.; Konstantatos, G. Stabilization of Environmentally-Friendly Cs_2TiBr_6 Perovskite Nanocrystals with $SnBr_4$. *Chem. Comm.* **2023**, *59* (37), 5567–5570. https://doi.org/10.1039/D3CC00581J.

(27) Ju, M. G.; Chen, M.; Zhou, Y.; Garces, H. F.; Dai, J.; Ma, L.; Padture, N. P.; Zeng, X. C. Earth-Abundant Nontoxic Titanium(IV)-Based Vacancy-Ordered Double Perovskite Halides with Tunable 1.0 to 1.8 EV Bandgaps for Photovoltaic Applications. *ACS Energy Lett.* **2018**, *3* (2), 297–304. https://doi.org/10.1021/acsenergylett.7b01167.

(28) Kupfer, C.; Elia, J.; Kato, M.; Osvet, A.; Brabec, C. J. Mechanochemical Synthesis of Cesium Titanium Halide Perovskites $Cs_2TiBr_{6-x}I_x$ (x = 0, 2, 4, 6). *Crystal Research and Technology* **2022**, 2200150. https://doi.org/10.1002/crat.202200150.

(29) Abate, A. Perovskite Solar Cells Go Lead Free. *Joule* **2017**, *1*(4), 659–664. https://doi.org/10.1016/j.joule.2017.09.007.

(30) Saparov, B.; Sun, J. P.; Meng, W.; Xiao, Z.; Duan, H. S.; Gunawan, O.; Shin, D.; Hill, I. G.; Yan, Y.; Mitzi, D. B. Thin-Film Deposition and Characterization of a Sn-Deficient Perovskite Derivative Cs_2SnI_6. *Chemistry of Materials* **2016**, *28* (7), 2315–2322. https://doi.org/10.1021/acs.chemmater.6b00433.

(31) Karim, M. M. S.; Ganose, A. M.; Pieters, L.; Winnie Leung, W. W.; Wade, J.; Zhang, L.; Scanlon, D. O.; Palgrave, R. G. Anion Distribution, Structural Distortion, and Symmetry-Driven Optical Band Gap Bowing in Mixed Halide Cs_2SnX_6 Vacancy Ordered Double Perovskites. *Chemistry of Materials* **2019**, *31* (22), 9430–9444. https://doi.org/10.1021/acs.chemmater.9b03267.

(32) Maughan, A. E.; Ganose, A. M.; Bordelon, M. M.; Miller, E. M.; Scanlon, D. O.; Neilson, J. R. Defect Tolerance to Intolerance in the Vacancy-Ordered Double Perovskite Semiconductors Cs_2SnI_6 and Cs_2TeI_6. *J. Am. Chem. Soc.* **2016**, *138* (27), 8453–8464. https://doi.org/10.1021/jacs.6b03207.

(33) Maughan, A. E.; Ganose, A. M.; Candia, A. M.; Granger, J. T.; Scanlon, D. O.; Neilson, J. R. Anharmonicity and Octahedral Tilting in Hybrid Vacancy-Ordered Double Perovskites. *Chemistry of Materials* **2018**, *30* (2), 472–483. https://doi.org/10.1021/acs.chemmater.7b04516.

(34) Maughan, A. E.; Ganose, A. M.; Scanlon, D. O.; Neilson, J. R. Perspectives and Design Principles of Vacancy-Ordered Double Perovskite Halide Semiconductors. *Chemistry of Materials* **2019**, *31* (4), 1184–1195. https://doi.org/10.1021/acs.chemmater.8b05036.

(35) Maughan, A. E.; Ganose, A. M.; Almaker, M. A.; Scanlon, D. O.; Neilson, J. R. Tolerance Factor and Cooperative Tilting Effects in Vacancy-Ordered Double Perovskite Halides. *Chemistry of Materials* **2018**, *30* (11), 3909–3919. https://doi.org/10.1021/acs.chemmater.8b01549.

(36) Ouyang, R. Exploiting Ionic Radii for Rational Design of Halide Perovskites. *Chemistry of Materials* **2020**, *32* (1), 595–604. https://doi.org/10.1021/acs.chemmater.9b04472.

(37) Lu, C.; Wright, M. W.; Ma, X.; Li, H.; Itanze, D. S.; Carter, J. A.; Hewitt, C. A.; Donati, G. L.; Carroll, D. L.; Lundin, P. M. et al. Cesium Oleate Precursor Preparation for Lead Halide Perovskite Nanocrystal Synthesis: The Influence of Excess Oleic Acid on Achieving Solubility, Conversion, and Reproducibility. *Chemistry of Materials* **2019**, *31* (1), 62–67. https://doi.org/10.1021/acs.chemmater.8b04876.

(38) Zunger, A.; Wei, S. H.; Ferreira, L. G.; Bernard, J. E. Special Quasirandom Structures. *Phys. Rev. Lett.* **1990**, *65* (3). https://doi.org/10.1103/PhysRevLett.65.353.

(39) Huang, Y. T.; Kavanagh, S. R.; Righetto, M.; Rusu, M.; Levine, I.; Unold, T.; Zelewski, S. J.; Sneyd, A. J.; Zhang, K.; Dai, L. et al. Strong Absorption and Ultrafast Localisation in $NaBiS_2$ Nanocrystals with Slow Charge-Carrier Recombination. *Nat. Commun.* **2022**, *13* (1). https://doi.org/10.1038/s41467-022-32669-3.

(40) Ångqvist, M.; Muñoz, W. A.; Rahm, J. M.; Fransson, E.; Durniak, C.; Rozyczko, P.; Rod, T. H.; Erhart, P. ICET – A Python Library for Constructing and Sampling Alloy Cluster Expansions. *Adv. Theory Simul.* **2019**, *2* (7). https://doi.org/10.1002/adts.201900015.

(41) Van De Walle, A.; Tiwary, P.; De Jong, M.; Olmsted, D. L.; Asta, M.; Dick, A.; Shin, D.; Wang, Y.; Chen, L. Q.; Liu, Z. K. Efficient Stochastic Generation of Special Quasirandom Structures. *CALPHAD* **2013**, *42*, 13–18. https://doi.org/10.1016/j.calphad.2013.06.006.

(42) Kresse, G.; Furthmü, J. Efficient Iterative Schemes for Ab Initio Total-Energy Calculations Using a Plane-Wave Basis Set. *Phys. Rev. B* **1996**, *54* (16). https://doi.org/10.1103/PhysRevB.54.11169.

(43) Blochl, P. E. Projector Augmented-Wave Method. *Phys. Rev. B* **1994**, *50* (24). https://doi.org/10.1103/PhysRevB.50.17953.

(44) Heyd, J.; Scuseria, G. E.; Ernzerhof, M. Hybrid Functionals Based on a Screened Coulomb Potential. *J. Chem. Phys.* **2003**, *118* (18), 8207–8215. https://doi.org/10.1063/1.1564060.

(45) Grimme, S.; Antony, J.; Ehrlich, S.; Krieg, H. A Consistent and Accurate Ab Initio Parametrization of Density Functional Dispersion Correction (DFT-D) for the 94 Elements H-Pu. *J. Chem. Phys.* **2010**, *132* (15). https://doi.org/10.1063/1.3382344.

(46) Grimme, S.; Ehrlich, S.; Goerigk, L. Effect of the Damping Function in Dispersion Corrected Density Functional Theory. *J. Comput. Chem.* **2011**, *32* (7), 1456–1465. https://doi.org/10.1002/jcc.21759.

(47) S. R. Kavanagh. *github.com/kavanase/vaspup2.0*. https://github.com/kavanase/vaspup2.0 (accessed 2023-07-14).

(48) Cucco, B.; Bouder, G.; Pedesseau, L.; Katan, C.; Even, J.; Kepenekian, M.; Volonakis, G. Electronic Structure and Stability of Cs_2TiX_6 and Cs_2ZrX_6 (X=Br,I) Vacancy Ordered Double Perovskites. *Appl. Phys. Lett.* **2021**, *119* (18). https://doi.org/10.1063/5.0070104.

(49) Ganose, A. M.; Jackson, A. J.; Scanlon, D. O. Sumo: Command-Line Tools for Plotting and Analysis of Periodic Ab Initio Calculations. *J. Open Source Softw.* **2018**, *3* (28), 717. https://doi.org/10.21105/joss.00717.

(50) Zhu, B.; Kavanagh, S. R. *github.com/SMTG-UCL/easyunfold*. https://github.com/SMTG-UCL/easyunfold (accessed 2023-09-14).

(51) S. R. Kavanagh. *github.com/SMTG-UCL/doped*. https://github.com/SMTG-UCL/doped (accessed 2023-07-14).

(52) Jain, A.; Ong, S. P.; Hautier, G.; Chen, W.; Richards, W. D.; Dacek, S.; Cholia, S.; Gunter, D.; Skinner, D.; Ceder, G.; Persson, K. A. Commentary: The Materials Project: A Materials Genome Approach to Accelerating Materials Innovation. *APL Materials* **2013**, *1* (1). https://doi.org/10.1063/1.4812323.

(53) Ong, S. P.; Richards, W. D.; Jain, A.; Hautier, G.; Kocher, M.; Cholia, S.; Gunter, D.; Chevrier, V. L.; Persson, K. A.; Ceder, G. Python Materials Genomics (Pymatgen): A Robust, Open-Source Python Library for Materials Analysis. *Comput. Mater. Sci.* **2013**, *68*, 314–319. https://doi.org/10.1016/j.commatsci.2012.10.028.

(54) Wang, V.; Xu, N.; Liu, J. C.; Tang, G.; Geng, W. T. VASPKIT: A User-Friendly Interface Facilitating High-Throughput Computing and Analysis Using VASP Code. *Comput. Phys. Commun.* **2021**, *267*, 108033. https://doi.org/10.1016/j.cpc.2021.108033.

(55) A. J. Jackson. *github.com/ajjackson/mctools*. github.com/ajjackson/mctools (accessed 2023-07-14).

(56) Morgan, B. J. Vasppy. https://doi.org/10.5281/zenodo.8348189

(57) Shannon, R. D. Revised Effective Ionic Radii and Systematic Studies of Interatomic Distances in Halides and Chaleogenides. *Acta Cryst.* **1976**, *32* (5), 751-767. https://doi.org/10.1107/S0567739476001551.

(58) Liu, D.; Zha, W.; Yuan, R.; Chen, J.; Sa, R. A First-Principles Study on the Optoelectronic Properties of Mixed-Halide Double Perovskites $Cs_2TiI_{6-x}Br_x$. *New Journal of Chemistry* **2020**, *44* (32), 13613–13618. https://doi.org/10.1039/d0nj02535f.

(59) Kaewmeechai, C.; Laosiritaworn, Y.; Jaroenjittichai, A. P. First-Principles Study on Structural Stability and Reaction with H_2O and O_2 of Vacancy-Ordered Double Perovskite Halides: Cs_2(Ti, Zr, Hf)X_6. *Results Phys.* **2021**, *25*, 104225. https://doi.org/10.1016/j.rinp.2021.104225.

(60) Lee, B.; Stoumpos, C. C.; Zhou, N.; Hao, F.; Malliakas, C.; Yeh, C. Y.; Marks, T. J.; Kanatzidis, M. G.; Chang, R. P. H. Air-Stable Molecular Semiconducting Iodosalts for Solar Cell Applications: Cs_2SnI_6 as a Hole Conductor. *J. Am. Chem. Soc.* **2014**, *136* (43), 15379–15385. https://doi.org/10.1021/ja508464w.

(61) Xiong, Y.; Mathew, M.; Griffin, S. M.; Sipahigil, A.; Hautier, G. Midgap State Requirements for Optically Active Quantum Defects. *ArXiv preprint* **2023**, *2302* (10767). https://doi.org/10.48550/arXiv.2302.10767.

TOC graphic